



Synthesis of well-ordered MCM-41 containing highly-dispersed NiO nanoparticles and efficient catalytic epoxidation of styrene

KAI HUANG*, ZHILI WANG and DONGFANG WU

School of Chemistry and Chemical Engineering, Southeast University, Jiangning District, Nanjing 211189, China

E-mail: huangk@seu.edu.cn

MS received 5 January 2018; revised 11 April 2018; accepted 11 April 2018; published online 1 June 2018

Abstract. Well-ordered MCM-41 materials with different loadings of NiO were prepared combining hydrothermal method using cetyltrimethylammonia bromide as the structure-directing agent in an ammonia aqueous solution with calcination. A series of characterization of the resulting samples revealed that the materials maintained ordered mesostructure of MCM-41 after loading NiO and NiO nanoparticles were highly dispersed in the mesoporous wall and on the external surface of MCM-41. Characterization results also unveiled that Ni²⁺ prefer to enter the pores that formed by silicone gel during the hydrothermal reaction and incorporated into the pore wall and then formed NiO during the calcination process. And the TEM images indicated that smaller size NiO nanoparticles are easier to be formed on the MCM-41 materials. Catalytic results revealed that NiO should be the catalytic active centers for the oxidation of styrene and Ni-based materials showed the efficient catalytic property.

Keywords. NiO/MCM-41; heterogeneous catalysis; styrene; epoxidation.

1. Introduction

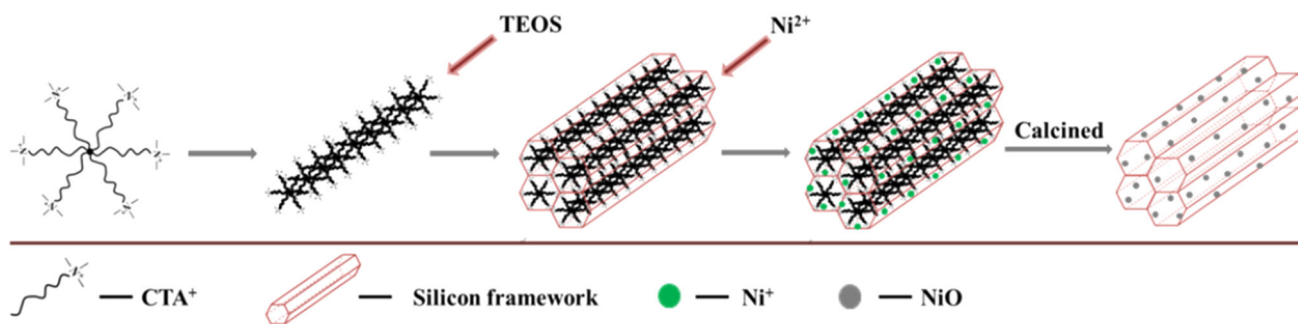
Nowadays, transition metal oxide catalyst such as nickel oxide,¹ cobalt oxide,² copper oxide,³ manganese oxide,⁴ vanadium oxide,⁵ molybdenum oxide,⁶ bimetallic oxide⁷ and polymetallic oxide⁸ are widely synthesized and used. Among these oxides, nickel oxide is a binary transition metal oxide with a wide range of applications as a p-type semiconductor with a wide band gap.⁹ In particular, due to the effect of quantum confinement, the nickel oxide with nanostructure shows excellent optical, magnetic and electronic properties. Owing to its high theoretical specific capacitance, nickel oxide is also a promising material as an electrode of supercapacitor.¹⁰ Furthermore, nickel oxide can also be applied to catalyze the oxidation of CO, methanol and hydrazine,¹¹ epoxidation of styrene and cyclooctene,¹² decomposition of ethanol,¹³ dehydrogenations of ethane,¹⁴ etc.

However, since the nanoparticle would easily be aggregated into large bulk, quantum-confined nickel oxide nanoparticles, especially the highly-dispersed nickel oxide nanoparticles, tend to be difficult to obtain during synthesis.¹⁵ Therefore, in the process of catalyst

synthesis, a support is necessary to disperse the nanoparticles to prevent agglomeration. Mesoporous silica is well-known for its high specific surface area, high porosity and oriented channels, which are the characteristics of ideal catalyst support materials.¹⁶ Particularly, mesoporous MCM-41 is a promising support because of its large surface area, high thermal stability and large pore size.¹⁷

Numerous studies have revealed that NiO as an active phase showed a superior catalytic performance in olefin epoxidation.¹⁸ Additionally, nickel complexes as active phase, supported over ordered mesoporous silica as catalysts for olefin epoxidation, have also been reported.¹⁹ Styrene oxide is an important intermediate for a large variety of fine chemicals.²⁰ So catalytic oxidation of styrene to styrene oxide is significant from both academic and commercial point of view. NiO supported on Al₂O₃²¹ has been used as a catalyst for epoxidation of styrene. However, due to the fact that the specific surface area of Al₂O₃ is not high enough (336.7 m²/g), NiO was not highly dispersed, resulting in the conversion of styrene to only 60.2%. Therefore, using materials with higher specific surface area as support could improve the catalytic activity of the catalyst.

*For correspondence



Scheme 1. The schematic illustration for the synthetic route of xNi-MCM-41.

Considering this, we chose MCM-41 with the high specific surface area as support and synthesized supported catalysts with different nickel oxide loadings *via* the method of combining hydrothermal with calcination. The catalysts were used to catalyze epoxidation of styrene, and to the best of our knowledge, using nickel modified MCM-41 as a catalyst for the selective epoxidation of styrene has not been reported.

Herein, we proposed a novel templating self-assembly route based on the electrostatic assembly mechanism, and the route could illustrate the formation mechanism of the hexagonal channel in MCM-41 adequately. Scheme 1 illustrates the process, formation of micelles by surfactants dispersed in water, and subsequently rod-like micelles due to the aggregation of micelles. Afterwards, the addition of silicon source resulted in the self-assembly of micelles and the formation of the hexagonal outline. Then, electronegative silicate oligomers would match with electropositive ions in the tail of the micelles and an inorganic silicon wall formed on the surface of the organic hexagonal prism, eventually. After that, Ni[2+] anchored on the surface of silicon gel entered the pores that are formed by silicone gel under the effect of surfactant during the hydrothermal reaction and formed highly-dispersed NiO nanoparticles on the surface and pore wall of MCM-41 material during the calcination process.

2. Experimental

2.1 Materials and synthetic procedures

Tetraethyl orthosilicate (TEOS, AR), cetyltrimethyl ammonium bromide (CTAB, AR), ammonia (25%, AR), nickel nitrate hexahydrate ($\text{Ni}(\text{NO}_3)_2 \cdot 6\text{H}_2\text{O}$, AR), acetonitrile (CH_3CN , AR) and tert-butyl hydroperoxide (TBHP, AR) were purchased from Sinopharm Chemical Reagent Co., Ltd. Styrene (C_8H_8 , AR) was purchased from Shanghai Macklin Biochemical Co., Ltd.

A typical synthetic process for the preparation of modified MCM-41 follows the reported procedures²² with minor modification. In a typical synthesis, 2.62 g of CTAB was dissolved in 125 mL of deionized water, and then 36 mL of 25% ammonia was added to the solution under vigorous stirring. Then, 14 mL of TEOS was slowly added to the above solution. After 0.5 h of stirring at 35 °C and the hydrolysis of TEOS was complete, the resulting solution turned milk-white, then different amounts of $\text{Ni}(\text{NO}_3)_2 \cdot 6\text{H}_2\text{O}$ (2, 4, 6 mmol) as nickel source were dissolved in deionized water and were added to the above solutions, respectively. After that, the resulting gel was allowed to crystallize at 110 °C for 52 h in a Teflon-lined autoclave. The sample was filtered, washed with deionized water up to neutral pH, and dried at 60 °C for 12 h. Finally, the resultant powder was calcined at 550 °C for 6 h. The samples corresponding to different nickel amount were labelled as xNi-MCM-41, in which x stands for the amount of nickel in different samples.

For comparison, pure MCM-41 was synthesized *via* the above procedure without the addition of nickel source. Pure NiO nanoparticles were also synthesized by following the procedures of preparing Ni-base MCM-41 without adding TEOS.

2.2 Characterization methods

Crystalline phases of the catalysts were measured by X-ray Diffraction (XRD) with a $\text{CuK}\alpha$ radiation source ($\lambda = 0.15406$ nm, Smartlab, Rigaku). The X-ray tubes worked at 40 kV and 30 mA. The small angle XRD was recorded over the 2θ range of $1 - 10^\circ$ with a step size of 0.02° at an acquisition time of 0.4 s. The wide-angle XRD was collected over the 2θ range from 10° to 80° with a step size of 0.1° at a collection time of 0.3 s. Crystal phases were identified by Joint Committee on Powder Diffraction Standards (JCPDS) files.

Textural properties of the samples were derived from N_2 adsorption/desorption measurement at 77 K on Quadrasorb SI 2MP. Prior to the measurement, the samples were out-gassed at 150 °C for 12 h. The average pore diameter and pore size distribution curves were established from the adsorption branches of isotherms using the Barrett-Joyner-Halenda (BJH) method.

Surface morphology of the catalysts was examined by transmission electron microscopy (TEM) (Tecnai-G20, FEI)

and operated at an accelerating voltage of 200 kV. The samples were dispersed ultrasonically in ethanol and then deposited on a TEM copper grid before the measurement.

The loadings of nickel in catalysts were measured using Inductively Coupling Plasma spectrometer (ICP) (Spectroblue ICP-OES). Fourier transform infrared (FT-IR) spectra were recorded in the range of 400–4000 cm⁻¹ on Thermo Fisher Nicolet 5700 spectrophotometer in KBr pellets. UV-Vis diffuse reflectance Spectrometer (DRS) (UV-2600, Shimadzu) equipped with a diffuse reflectance accessory was used. The spectra were recorded in the range 200–800 nm at room temperature.

Surface chemical composition of the samples was investigated by X-ray photoelectron spectroscopy (XPS) (K-Alpha, Thermo Fisher) equipped with a standard Al K α excitation source (1486.6 eV). The C1s peak at 284.6 eV was used as the reference for binding energies.

The reduction behavior of the prepared materials was investigated by hydrogen temperature-programmed reduction (TPR) measurement on a chemisorption analyzer (Micor 2920, Micromeritics) equipped with a thermal conductivity detector (TCD). TPR is a convenient technique for studying the reduction behavior of supported oxide materials reducible at different temperature intervals. Before the TPR analysis, the carbonate and hydrate' impurities were removed by flowing argon over the catalyst at a flow rate of 30 mL/min at 300 °C for 1 h and the system was then cooled to room temperature. The amount of H₂ uptake during the reduction was measured continuously using TCD.

2.3 Catalytic activity measurements

The epoxidation of styrene reaction was carried out in a 50 mL two-necked flask equipped with a condenser. Generally, 1041.5 mg styrene, 7.9 mg acetonitrile and 50 mg catalyst were added to a 50 mL two-necked flask, then 10 mmol

tert-butyl hydroperoxide as oxidant was added. Finally, the reaction began after immersing the flask into oil bath, and kept at 80 °C. The reaction was carried out under magnetic stirring. The products of epoxidation were analyzed by a gas chromatograph (INESA GC-126) equipped with OV-1701 capillary column and a FID detector with toluene as internal standard. The characterization of the main and by-products were performed by comparison of their retention times with standard samples. The alkene conversion and selectivity of products were calculated from peak area by standard addition method using Eqs. (1) and (2), respectively:

$$\text{Conversion (\%)} = \frac{\text{mole of reactant converted}}{\text{mole of the reactant in feed}} \times 100 \quad (1)$$

$$\begin{aligned} \text{Product selectivity (\%)} &= \frac{\text{mole of the product formed}}{\text{mole of the reactant converted}} \times 100 \\ & \quad (2) \end{aligned}$$

In a typical experiment, after recovering the catalyst from the reaction mixture at optimum conditions, it was washed several times with acetonitrile and dried, and then reused under the same conditions for catalyst reusability test.

3. Results and Discussion

3.1 Structure and morphology

The X-ray powder diffraction measurement was used to characterize the crystallographic structure of the synthesized materials. The small-angle XRD patterns of samples are shown in Figure 1A. An intense main diffraction peak and two small peaks were well-resolved at 2.1°, 3.6° and 4.2°, corresponding to the (111), (200) and (220) planes, which are the characteristics of the

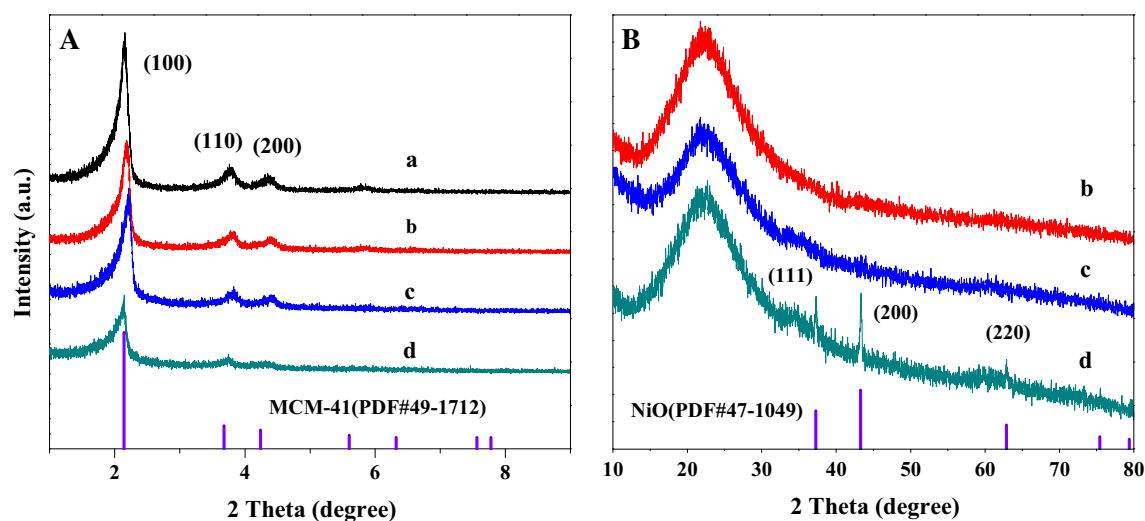


Figure 1. Small-angle (A) and large-angle (B) XRD patterns of samples: (a) MCM-41, (b) 2Ni-MCM-41, (c) 4Ni-MCM-41, (d) 6Ni-MCM-41.

Table 1. The textural properties of samples.

Materials	Ni/Si ^a		d ₁₀₀ (nm)	a ₀ ^b (nm)	S _{BET} (m ² /g)	Pore volume ^c (cm ³ /g)	Pore size ^d (nm)	W _d ^e (nm)
	Initial mixture	Product						
MCM-41	–	–	3.92	4.53	795	0.86	2.80	1.73
2Ni-MCM-41	0.03	0.018	3.92	4.53	829	0.97	2.79	1.74
4Ni-MCM-41	0.06	0.045	3.84	4.43	767	1.10	2.78	1.65
6Ni-MCM-41	0.09	0.085	3.81	4.40	722	1.28	2.63	1.77

^aFrom ICP (molar ratio).

^bHexagonal unit cell parameter.

^{c,d}Calculated from adsorption branch with BJH method.

^eW_d = a₀ - Pore size.

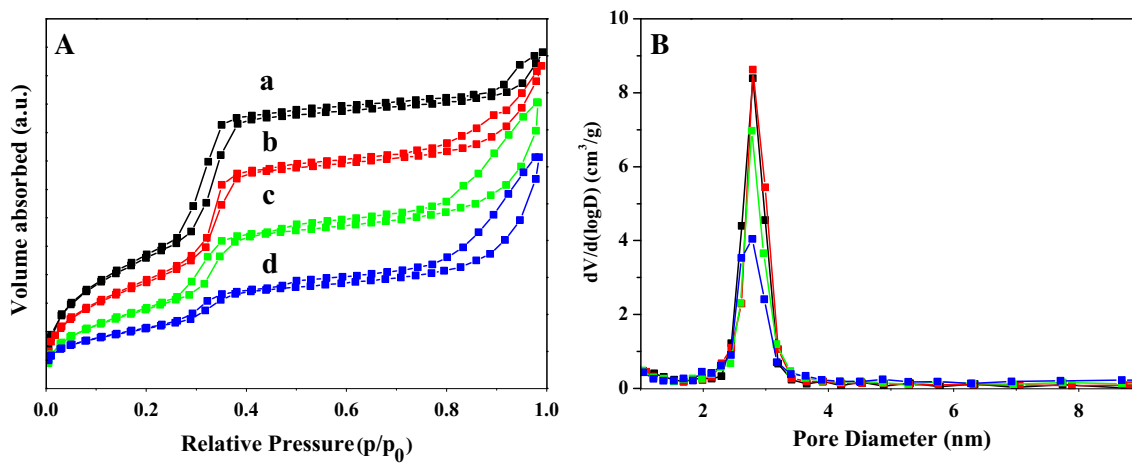


Figure 2. N₂ adsorption-desorption isotherms (A), and pore size distribution curve derived from the adsorption branch (V: pore volume, D: pore diameter) (B) for samples with different nickel oxide loadings: (a) MCM-41, (b) 2Ni-MCM-41, (c) 4Ni-MCM-41 and (d) 6Ni-MCM-41.

hexagonal pore mesostructure of the synthesized materials (JCPDS 49-1712).²³ Compared with pure MCM-41, the diffraction peak of Ni-based materials was shifted toward higher angles, indicating the decrease of d₁₀₀ interplanar spacing, which can be seen in the data in Table 1. The d₁₀₀ values were obtained from Jade 5.0 and the hexagonal unit cell parameter a₀ was calculated by the equation, $a_0 = 2d_{100}\sqrt{3}$. The increase of the d-values and a₀ can be attributed to the higher ionic radii of Ni²⁺ (69 pm) in comparison to Si⁴⁺ (40 pm) and due to the longer bond lengths of Ni-O in comparison to Si-O bonds,²⁴ suggesting the successful incorporation of NiO.

Furthermore, when the load of nickel was less than or equal to 4 mmol, there was no obvious change in the intensity of the peaks, indicating that the structural integrity was retained after modification. However, when the load of nickel reached 6 mmol, the intensity of the peaks weakened, especially for the intensity of (100) peak, indicating that the structures were retained but with a slight distortion of the channels.²⁵

In large-angle XRD patterns (Figure 1B), all samples showed a broad diffraction peak at 23°, which was ascribed to the amorphous framework of MCM-41.²⁶ And, 6Ni-MCM-41 revealed three peaks corresponding to (111), (200) and (220) reflections assigned to the crystalline NiO (JCPDS 47-1049). While for 4Ni-MCM-41, several weak peaks which are specific to nickel oxide were detected. As for 2Ni-MCM-41, the peak that corresponds to nickel oxide was hardly found, suggesting that no NiO nanoparticle was present on the external surface of MCM-41 materials or the micro-morphology grain formed was below the detection limit of XRD.²⁷ These results indicated that the emerging crystal diffraction peaks were accompanied by an enhanced trend with the increase of nickel loading in the samples, owing to the increment of crystallinity and enlargement of grain size for nickel oxide nanoparticles according to Scherrer's Equation.²⁸

To further investigate the textural information of all samples, the N₂ adsorption/desorption isotherms and pore size distributions were obtained and depicted in

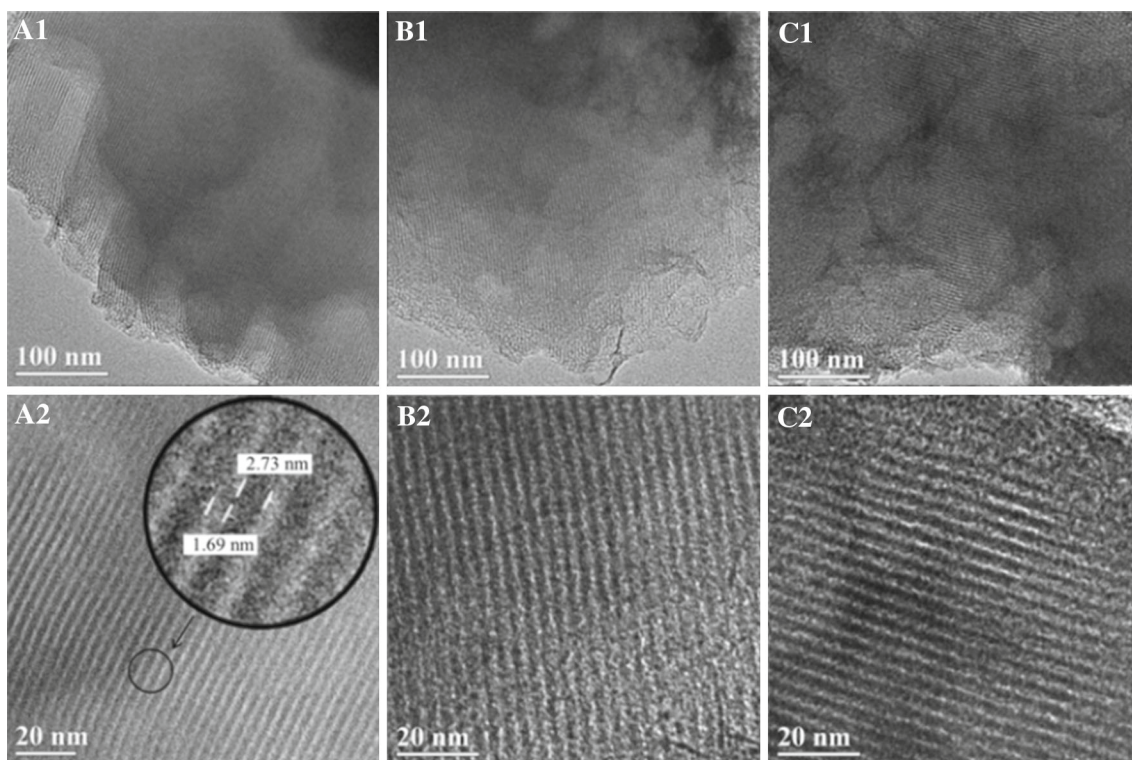


Figure 3. TEM images of MCM-41 (a₁ and a₂), 2Ni-MCM-41 (b₁ and b₂) and 4Ni-MCM-41 (c₁ and c₂).

Figure 2A and B, respectively. The surface areas were measured with the BET method, pore sizes were calculated from the adsorption branch by BJH method. The surface area, pore volume, pore size and wall thickness (W_d) are also summarized in Table 1. As observed in Figure 2A, all the samples exhibited typical IUPAC type IV adsorption isotherm with a H₁ type hysteresis loop, indicating that the mesostructure of the synthesized samples²⁹ and the incorporation of nickel oxide did not obviously destroy the mesophase of the samples. And along with the increase of nickel loading in the samples, the size of the hysteresis loop varied with an increasing trend, indicating a declining trend of pore size of samples (Table 1).

For all the samples, another common feature is that the sharp step over the narrow range of relative pressure at P/P_0 of 0.25–0.4 corresponded to the characteristic of capillary condensation inside the conventional mesoporous present in MCM-41 structure.³⁰ Upon nickel incorporation, the location of the inflection step remained the same, suggesting that all the samples kept ordered mesoporous structure (Figure 2B), while the sharpness turned flat and the adsorption amount decreased significantly, owing to the fact that the declining specific surface area (Table 1) restrained monolayer adsorption of nitrogen towards the walls of the mesopores.³¹ Furthermore, as shown in Figure 2B, all the

prepared materials were mesoporous with a narrow pore size distribution at the range of 2.5–3.5 nm. And the vertices of the curves all appeared at 2.75 nm, indicating that the number of pores with a diameter of 2.75 nm is the most.

The TEM images of the samples are shown in Figures 3 and 4. For MCM-41, the well-ordered mesopores and straight channel are clearly depicted. The diameter of mesopores was about 2.73 nm and the thickness of mesoporous wall was about 1.69 nm (inset Figure 3a₂), so the distance between two cylindrical mesopores was about 4.42 nm. The data is consistent with the data in Table 1. Compared to the pure MCM-41, Ni-based materials also showed well-ordered mesoporous channel with minor defects in mesoporous walls as a consequence of incorporation of nickel oxide nanoparticles in the walls. Moreover, NiO nanoparticles were not observed over 2Ni-MCM-41 and 4Ni-MCM-41, but the data from Table 1 confirms the presence of nickel and the molar ratio of nickel to silicon is very close to that of the initial mixture. NiO nanoparticles could be observed over 6Ni-MCM-41 (Figure 4B), and the results are consistent with XRD analysis.

The selected-area electron diffraction (SAED) pattern and the particle-size distribution of NiO nanoparticles are also shown in Figure 4. Diffraction rings assigned to the (111), (200), (220) and (311) planes of NiO

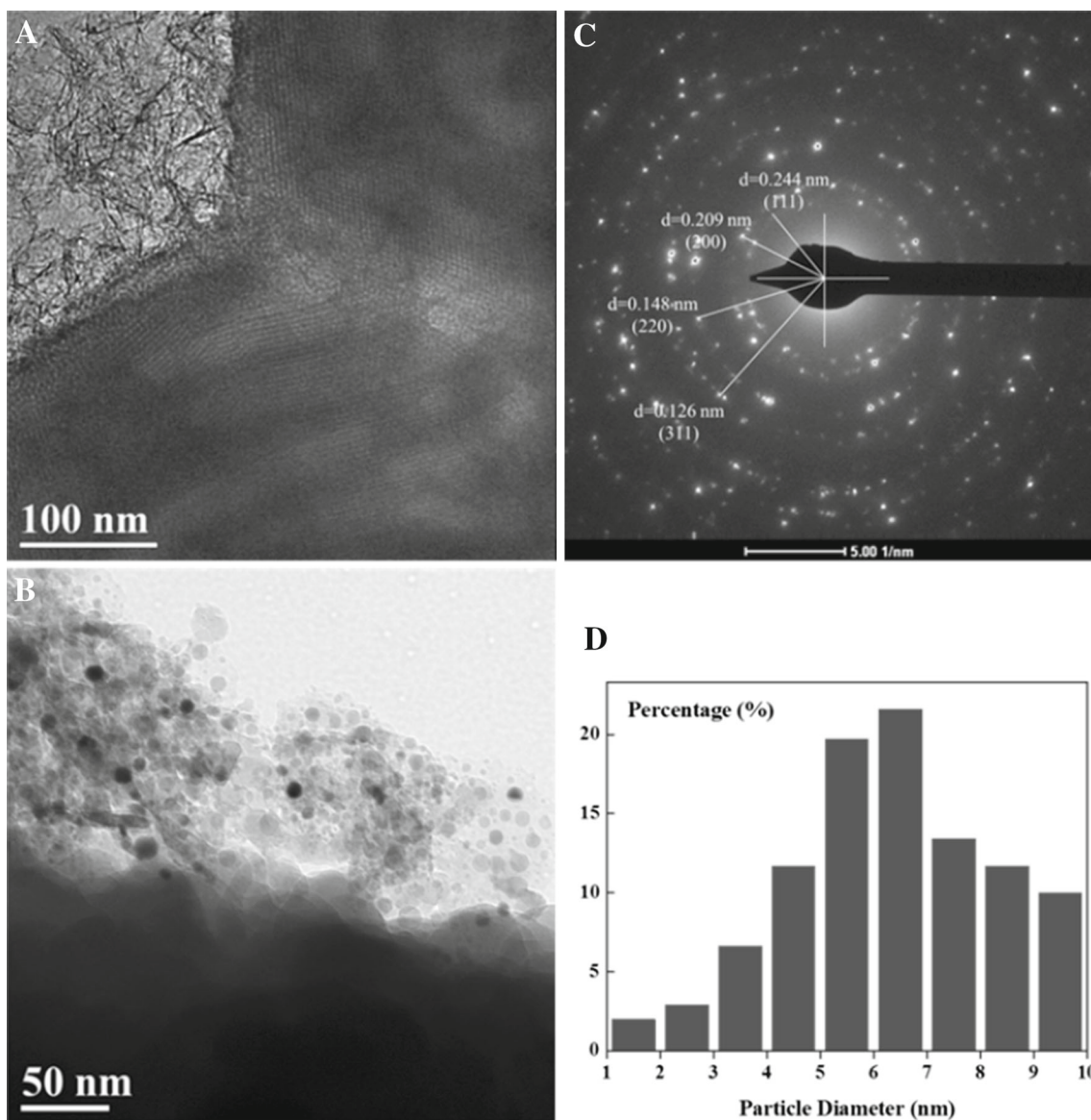


Figure 4. TEM images of 6Ni-MCM-41 (A and B) and SAED pattern (C), particle-size distribution of NiO nanoparticles (D).

nanocrystals are clearly seen in Figure 4C. As shown in Figure 4D, the particle size of the NiO nanoparticles varied from 1 to 10 nm, and the vast majority was in the 5–7 nm range.

The TEM image and XRD pattern of as-prepared pure NiO nanoparticles are presented in Figure 5. The sharp diffraction peaks (Figure 5B) are assigned to NiO nanocrystals (JCPDS 47-1049) which proved that the NiO with high crystallinity had been synthesized successfully. As shown in Figure 5A, the length and width of rod-like NiO nanoparticles are about 42 nm and 24 nm, respectively. While the maximum size of NiO nanoparticles supported on MCM-41 is only about 10 nm, which is much smaller than that of pure NiO nanoparticles,

indicating that the silicon source is beneficial to the formation of small size NiO nanoparticles.

3.2 State of nickel species

Figure 6 shows the FT-IR spectra of all samples in the region from 4000 to 400 cm^{-1} . The band at 3445 cm^{-1} observed in all samples are ascribed to the symmetrical stretching vibration of -OH groups on the surface of MCM-41 and the band at 1627 cm^{-1} is assigned to the bending vibration of adsorbed water.³² The bands at 1083 and 808 cm^{-1} are related to the asymmetric stretching vibration and symmetric stretching vibration of

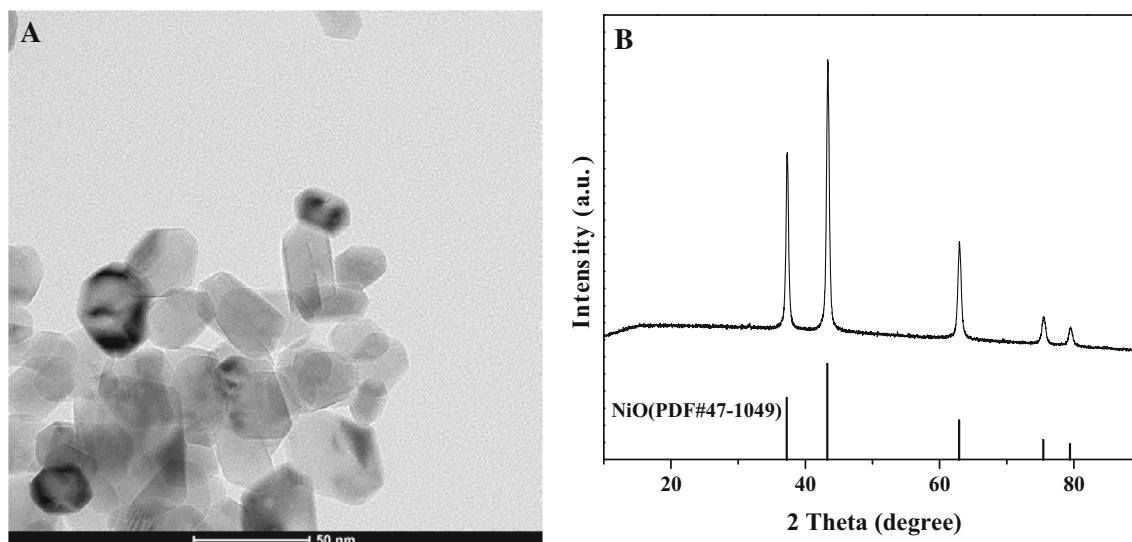


Figure 5. (A) TEM image and (B) XRD pattern of prepared NiO nanoparticles.

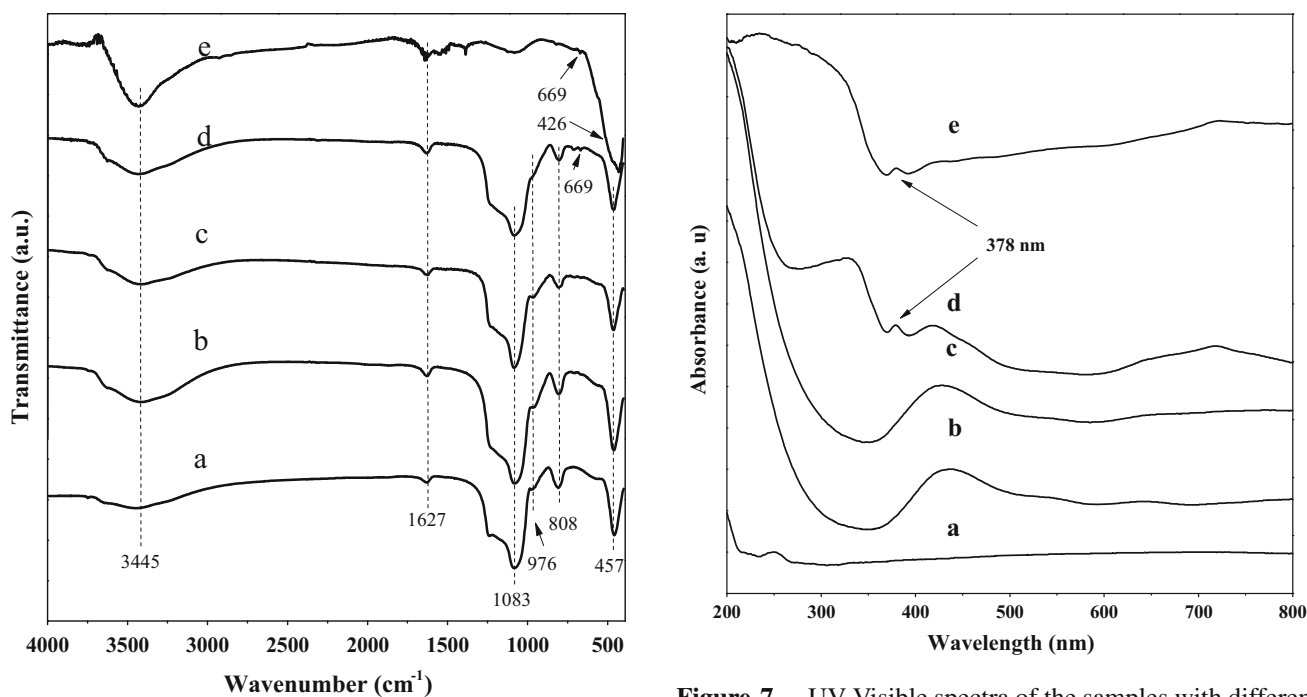


Figure 6. FT-IR spectra of samples with different nickel oxide loadings and NiO: (a) MCM-41, (b) 2Ni-MCM-41, (c) 4Ni-MCM-41, (d) 6Ni-MCM-41 and (e) NiO.

Si-O-Si in the framework of silica,³³ respectively. Additionally, the absorption bands at 976 cm^{-1} confirmed the presence of silanol group Si-OH and its symmetric stretching vibration;³⁴ moreover, the intensity of the absorption peaks showed a decreasing trend with increasing loading of nickel in these samples, suggesting the decreasing of surface Si-OH in the samples. That could be attributed to the fact that the nickel oxide nanoparticle incorporated in the silicate walls and interacted with the walls.³⁵ And the FT-IR bands at 457 cm^{-1}

Figure 7. UV-Visible spectra of the samples with different nickel oxide loadings: (a) MCM-41, (b) 2Ni-MCM-41, (c) 4Ni-MCM-41 and (d) 6Ni-MCM-41 and (e) NiO.

are related to the bending vibration of the rocking mode of Si-O-Si.³⁶

The presence of Ni=O stretching vibration was confirmed by the absorption band at 669 cm^{-1} , demonstrating the presence of NiO in MCM-41.³⁷ For comparison, the FT-IR of NiO is also depicted in Figure 6, and the band at 669 cm^{-1} was also observed in NiO, further confirming that NiO has been loaded into MCM-41. In addition, the absorption band at 426 cm^{-1} in NiO is assigned to the Ni-O vibration mode³⁸ which could be

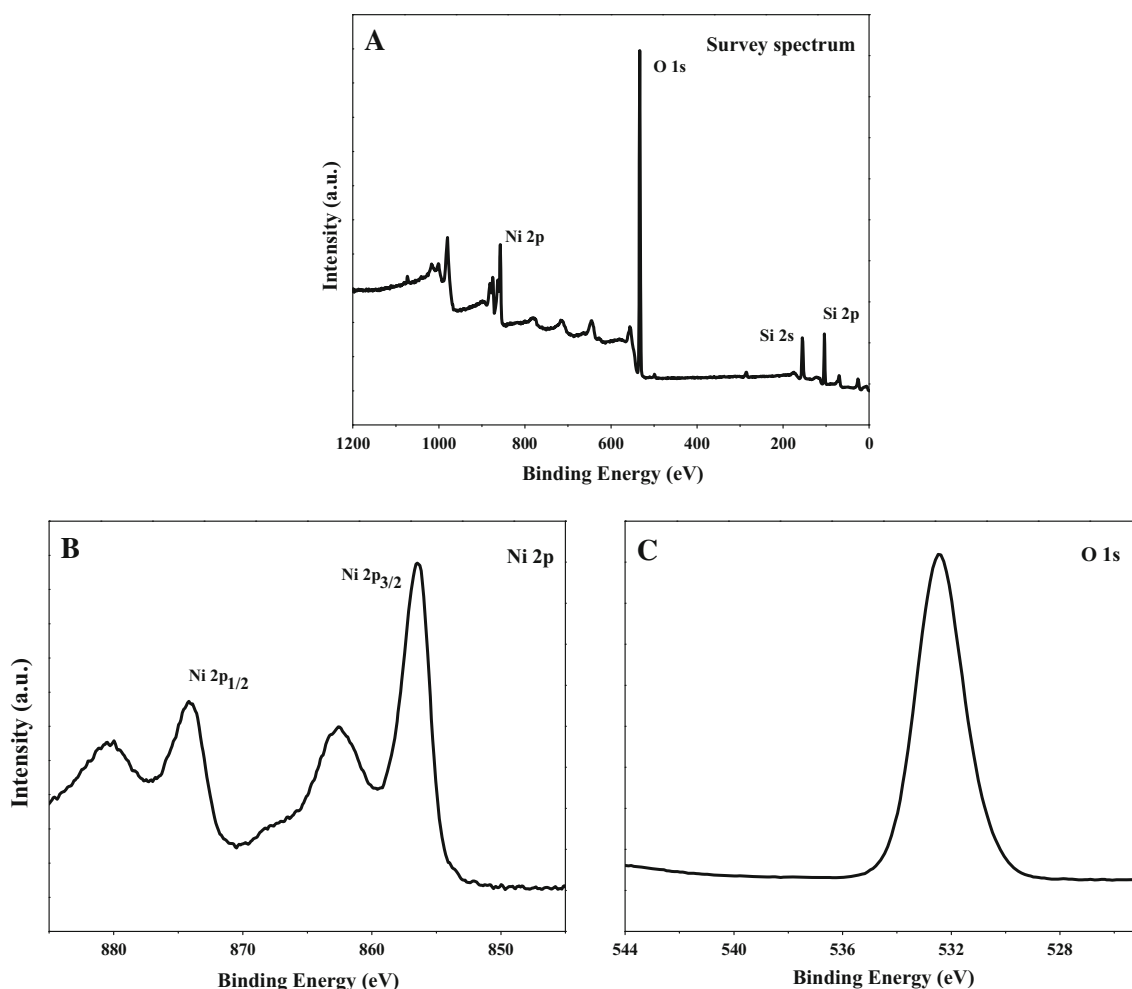


Figure 8. XPS spectra of 6Ni-MCM-41.

covered by the band at 457 cm^{-1} related to the bending vibration of the rocking mode of Si-O-Si in Ni-base MCM-41.

UV-Vis spectra of the samples are shown in Figure 7. A strong absorption in the UV region was observed at 378 nm in 6Ni-MCM-41, which approached the absorption at 360 nm and 364 nm, attributed to the band gap absorption in NiO that is reported in literature.³⁸ What is more, the as-synthesized NiO also showed the absorption at the same wavelength, confirming the presence of NiO in MCM-41. While the band was not found in other Ni-based materials, which could be due to the fact that the loading of NiO was too little to be detected. D deservedly, the parent MCM-41 showed no absorption assigned to NiO, either.

Figure 8 shows the XPS spectra of 6Ni-MCM-41, and the survey spectrum (Figure 8A) identified the presence of Ni, O and Si clearly. The high resolution Ni 2p XPS spectrum (Figure 8B) showed two prominent peaks at 874 and 856 eV, assigned to Ni 2p_{1/2} and Ni 2p_{3/2} states of Ni²⁺ in NiO,³⁹ respectively. And the peak at 880 eV

corresponded to the satellite peak of Ni 2p_{1/2}, while the peak at 862 eV is assigned to the satellite peak of Ni 2p_{3/2}.⁴⁰ Besides, as shown in Figure 8C, the peak centered at 532 eV could be attributed to the binding energy of O 1s, which is ascribed the O²⁻ in the NiO.⁴¹ All these results confirmed the presence of NiO.

H₂-TPR technique was adopted to study the reduction behavior of supported NiO materials. The H₂-TPR curve of 6Ni-MCM-41 is shown in Figure 9. 6Ni-MCM-41 materials exhibited two reduction peaks at about 360 °C and 600 °C. The peak at 360 °C could be assigned to the reduction of the NiO on the external surface of MCM-41 materials, and the other peak at 600 °C could be ascribed to the reduction of the NiO in the mesoporous walls of MCM-41 materials. According to some literature, the reduction peak at 600 °C could be related to nickel oxide layer that interacted strongly with silicate surface.⁴² Additionally, the peak at 600 °C was much higher than that of 360 °C, indicating that the content of NiO on the external surface of MCM-41 was much less than the NiO in the mesoporous walls

of MCM-41 material. That is because of the fact that Ni^{2+} prefers to enter the pores formed by silicone gel under the effect of capillarity during the hydrothermal reaction and incorporated into the pore wall which then formed NiO during the calcination process. That could also explain above analysis results. As for 2Ni-MCM-41 and 4Ni-MCM-41, the content of Ni^{2+} was so little that all Ni^{2+} were incorporated into pore wall and highly dispersed NiO nanoparticles were formed eventually, so there was no NiO nanoparticle on the external surface of MCM-41 material, and hence NiO could not be detected. While for 6Ni-MCM-41, there was enough NiO present on the external surface of MCM-41 to be detected.

3.3 Catalytic results

The catalytic properties of all samples were evaluated by the liquid-phase epoxidation of styrene using *tert*-butyl hydroperoxide as oxidant and the corresponding catalytic results are presented in Table 2. For comparison, the catalytic properties of pure MCM-41 and NiO NPs were also investigated. As we can see, pure MCM-41 showed no catalytic activity towards the epoxidation of styrene, while NiO nanoparticles exhibited good catalytic activity, suggesting that nickel oxide should be the active centers for oxidation of styrene. But, as for 2Ni-MCM-41 and 4Ni-MCM-41, the conversion of styrene was poor as compared to NiO NPs although the selectivity of styrene oxide increased to a certain extent. That may be due to the fact that the loading of NiO was too little to achieve excellent catalytic effect, and the catalytic performance of 6Ni-MCM-41 mentioned below confirmed that. Owing to high dispersion of nickel oxide on the support and the synergistic effect between NiO nanoparticles and the supports, 6Ni-MCM-41 gave higher conversion and selectivity compared to pure NiO nanoparticles. What is more, a conclusion that NiO nanoparticles with smaller size possessed better catalytic performance, which can be understood by considering the size of NiO nanoparticles supported on MCM-41 was much smaller than that of pure NiO nanoparticles. The catalytic performance of 6Ni-MCM-41 was also better than that of other supported nickel oxide catalysts (Table 2).

For heterogeneous catalysts, catalyst reusability is an important parameter. So, the reusability of 6Ni-MCM-41 catalyst was investigated considering it exhibited the best catalytic performance among all the catalysts. The results are shown in Figure 10A. For comparison, the reusability of pure NiO nanoparticles was also investigated and the results are shown in Figure 10B. As displayed in Figure 10A, a sustainable catalytic activity

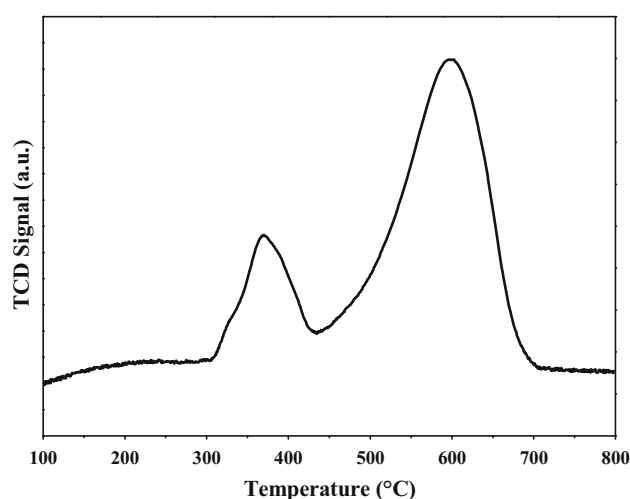


Figure 9. H_2 -TPR pattern of 6Ni-MCM-41.

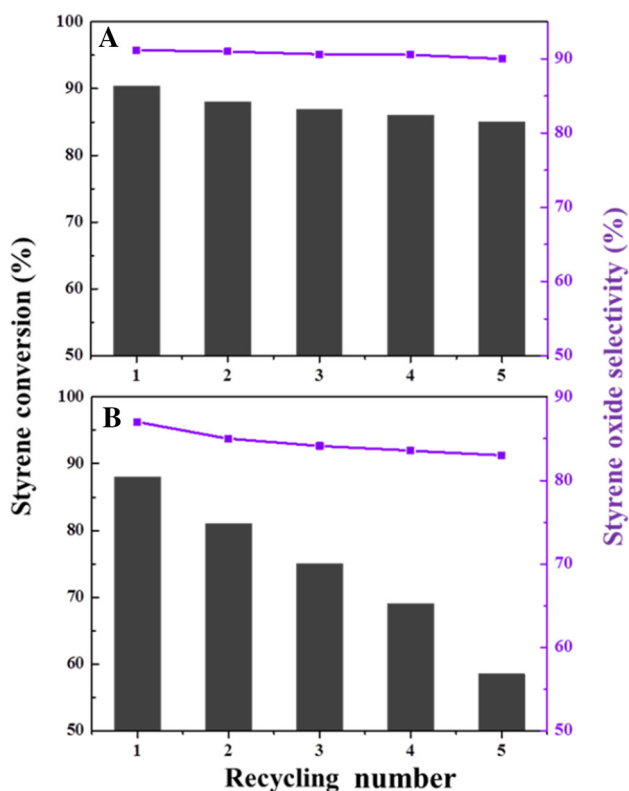


Figure 10. Reusability of 6Ni-MCM-41 (A) and pure NiO nanoparticles (B) catalysts in the epoxidation of styrene with TBHP.

was obtained even after five recycling experiments, indicating that 6Ni-MCM-41 had good stability attributed to the special interaction between nickel oxide and support. While pure NiO nanoparticles showed obvious reduction of the conversion efficiency, the selectivity of styrene oxide stayed at a high level. That could be due to the agglomeration of NiO nanoparticles without the support and dispersion in MCM-41 material.

Table 2. The catalytic performance of all the samples in the epoxidation of styrene ^a

Samples	Conversion (%)	S _{so} ^b (%)	S _{bza} ^c (%)	Ref.
Pure MCM-41	0	—	—	This study
NiO NPs	86.91	86.97	13.03	This study
2Ni-MCM-41	58.39	90.03	9.97	This study
4Ni-MCM-41	75.00	89.76	10.24	This study
6Ni-MCM-41	90.38	91.17	8.83	This study
NiO-Al ₂ O ₃	60.2	52.0	8.2	1
NiO-SiO ₂	49.8	61.9	1.0	6
NiO-In ₂ O ₃	33.0	29.0	0.5	

^aReaction conditions: 10 mmol styrene, 10 mL acetonitrile, 50 mg catalyst, 10 mmol tert-butyl hydroperoxide, 80 °C, 10 h, reflux.

^bso = styrene oxide.

^cbza = benzaldehyde.

4. Conclusions

In this paper, well-ordered MCM-41 containing highly-dispersed NiO nanoparticles in mesoporous walls and on the surface was synthesized successfully. A novel templating self-assembly route that could illustrate the formation mechanism of hexagonal channel in MCM-41 adequately is proposed. The characterization results revealed that Ni²⁺ prefers to enter the pores that are formed by silicone gel under the effect of capillarity during the hydrothermal reaction and smaller size NiO nanoparticles are easier to be formed on the MCM-41 materials. Additionally, catalytic results indicated that NiO is the catalytic active center for the oxidation of styrene and the efficient catalytic property of 6Ni-MCM-41 is attributed to high dispersion of nickel oxide on the support.

Acknowledgements

This work was supported by the National Natural Science Foundation of China (No. 21576049) and the Fundamental Research Funds for the Central Universities (No. 2242016K40082).

References

- (a) Yadav S K and Jeevanandam P 2014 Synthesis of NiO-Al₂O₃ nanocomposites by sol-gel process and their use as catalyst for the oxidation of styrene *J. Alloy. Compd.* **610** 567; (b) Ebadi A, Mozaffari M and Shojaei S 2014 Aerobic oxidation of cyclohexene catalyzed by NiO/MCM-41 nanocomposites in the gas phase *J. Chem. Sci.* **126** 989
- (a) Hassan H M A, Betiha M A, Elshaarawy R F M and El-Shall M Samy 2017 Promotion effect of palladium on Co₃O₄ incorporated within mesoporous MCM-41 silica for CO Oxidation *Appl. Surf. Sci.* **402** 99; (b) Li Z, Wu S, Yang C, Ma Y, Fu X, Peng L, Guan J and Kan Q 2017 Nano-Co₃O₄ supported on magnetic N-doped graphene as highly efficient catalyst for epoxidation of alkenes *Mol. Catal.* **432** 267
- Ghosh B K, Moitra D, Chandel M, Patra M K, Vadera S R and Ghosh N N 2017 CuO Nanoparticle Immobilised Mesoporous TiO₂-Cobalt Ferrite Nanocatalyst: A Versatile, Magnetically Separable and Reusable Catalyst *Catal. Lett.* **147** 1061
- (a) Qi B, Lou L, Yang Y, Wang Y, Bian W and Liu S 2014 Catalytic epoxidation of alkenes over supported manganese oxide with hydrogen peroxide: effect of supports and manganese loading *Res. Chem. Intermediat.* **40** 2973; (b) Skliri E, Papadogiorgakis S, Lykakis I N and Armatas G S 2017 Mesoporous Assembled Mn₃O₄ Nanoparticle Networks as Efficient Catalysts for Selective Oxidation of Alkenes and Aryl Alkanes *Chem. Plus. Chem.* **82** 136
- Ahmad A L, Koohestani B, Bhatia S and Ooi B S 2013 Mixed matrix vanadium oxide catalytic nanocomposite membrane for styrene oxidation *J. Sol-Gel Sci. Technol.* **67** 221
- Choudhary V, Jha R and Jana P 2008 Selective epoxidation of styrene to styrene oxide by TBHP using simple transition metal oxides (NiO, CoO or MoO₃) as highly active environmentally-friendly catalyst *Catal. Commun.* **10** 205
- Tang Y, Gao H, Yang M, Wang G and Li J 2016 NiO Promoted CuO-NiO/SBA-15 Composites as Highly Active Catalysts for Epoxidation of Olefins *New J. Chem.* **40** 8543
- Valand J, Parekh H and Friedrich H B 2013 Mixed Cu-Ni-Co nano-metal oxides: A new class of catalysts for styrene oxidation *Catal. Commun.* **40** 149
- Renaud A, Chavillon B, Cario L, Pleux L L and Szuwarski N 2013 Origin of the Black Color of NiO Used as Photocathode in p-Type Dye-Sensitized Solar Cells *J. Phys. Chem. C* **117** 22478
- (a) Zhang Y, Park M, Kim H Y and Park S 2017 Moderated surface defects of Ni particles encapsulated with NiO nanofibers as supercapacitor with high capacitance and energy density *J. Colloid Interf. Sci.* **500** 155; (b) Wang S, Li W, Xin L, Wu M, Sun W and Lou X 2017 Pollen-inspired synthesis of porous and hollow NiO

- elliptical microstructures assembled from nanosheets for high-performance electrochemical energy storage *Chem. Eng. J.* **321** 546
11. (a) Wang D, Yu H, Zhu Y and Song C 2017 NiO nanosheets rooting into Ni-doped CeO₂ microspheres for high performance of CO catalytic oxidation *Mater. Lett.* **198** 168; (b) Gu Z, Bin D, Feng Y, Zhang K, Wang J, Yan B, Li S, Xiong Z, Wang C, Shiraishi Y and Du Y 2017 Seed-mediated synthesis of cross-linked Pt-NiO nanochains for methanol oxidation *Appl. Surf. Sci.* **411** 379; (c) Hosseini S R, Ghasemi S and Kamali-Rousta M 2017 Preparation of CuO/NiO composite nanofibers by electrospinning and their application for electro-catalytic oxidation of hydrazine *J. Power Sources* **343** 467
 12. (a) Li T, Yang C, Rao X, Xiao F, Wang J and Su X 2015 Synthesis of magnetically recyclable Fe₃O₄@NiO nanostructures for styrene epoxidation and adsorption application *Ceram. Int.* **41** 2214; (b) Abbasi A, Soleimani M, Najafi M and Geranmayeh S 2017 Synthesis of nanostructured NiO/Co₃O₄ through thermal decomposition of a bimetallic (Ni/Co) metal-organic framework as catalyst for cyclooctene epoxidation *J. Mol. Struct.* **1133** 458
 13. Souza G D, Marcilio N R and Perez-Lopez O W 2017 Influence of the Ni/Al ratio on Ni-Al mixed oxides and their catalytic properties for ethanol decomposition *J. Therm. Anal. Calorim.* **128** 735
 14. Sanchis R, Delgado D, Agouram S, Soriano M D, Vázquez M I, Rodríguez-Castellón E, Solsona B and Nieto J M L 2017 NiO diluted in high surface area TiO₂ as an efficient catalyst for the oxidative dehydrogenation of ethane *Appl. Catal. A-Gen.* **536** 18
 15. Yang F, Zhou S, Gao S, Liu X, Long S and Kong Y 2017 In situ embedding of ultra-fine nickel oxide nanoparticles in HMS with enhanced catalytic activities of styrene epoxidation *Micropor. Mesopor. Mater.* **238** 69
 16. (a) Qian W, Wang H, Chen J and Kong Y 2015 Spherical V-Fe-MCM-48: The Synthesis, Characterization and Hydrothermal Stability *Materials* **8** 1752; (b) Wang G, Liu G, Xu M, Yang Z, Liu Z, Liu Y, Chen S and Wang L 2008 Ti-MCM-41 supported phosphotungstic acid: An effective and environmentally benign catalyst for epoxidation of styrene *Appl. Surf. Sci.* **255** 2632
 17. (a) Wang G, Liu G, Xu M, Yang Z, Liu Z, Liu Y, Chen S and Wang L 2008 Ti-MCM-41 supported phosphotungstic acid: An effective and environmentally benign catalyst for epoxidation of styrene *Appl. Surf. Sci.* **255** 2632; (b) Jyothi D, Deshpande P A, Venugopal B R, Chandrasekaran S and Madras G 2012 Transition metal oxide loaded MCM catalysts for photocatalytic degradation of dyes *J. Chem. Sci.* **124** 385; (c) Alibeik A M and Moaddeli A 2016 Cu-MCM-41 nanoparticles: An efficient catalyst for the synthesis of 5-substituted 1H-tetrazoles via [3+2] cycloaddition reaction of nitriles and sodium azide *J. Chem. Sci.* **128** 93
 18. (a) Yadav S K and Jeevanandam P 2014 Synthesis of NiO-Al₂O₃ nanocomposites by sol-gel process and their use as catalyst for the oxidation of styrene *J. Alloy. Compd.* **610** 567; (b) Tang Y, Gao H, Yang M, Wang G and Li J 2016 NiO Promoted CuO-NiO/SBA-15 Composites as Highly Active Catalysts for Epoxidation of Olefins *New J. Chem.* **40** 8543; (c) Li T, Yang C, Rao X, Xiao F, Wang J and Su X 2015 Synthesis of magnetically recyclable Fe₃O₄@NiO nanostructures for styrene epoxidation and adsorption application *Ceram. Int.* **41** 2214; (d) Wang G, Liu G, Xu M, Yang Z, Liu Z, Liu Y, Chen S and Wang L 2008 Ti-MCM-41 supported phosphotungstic acid: An effective and environmentally benign catalyst for epoxidation of styrene *Appl. Surf. Sci.* **255** 2632
 19. (a) Chakraborty J, Nandi M, Mayer F H, Sheldrick S W, Sorace L, Bhaumik A and Banerjee P 2007 Nickel Complexes with N₂O Donor Ligands: Syntheses, Structures, Catalysis and Magnetic Studies *Eur. J. Inorg. Chem.* **32** 5033; (b) Nandi M, Roy P, Uyama H and Bhaumik A 2011 Functionalized mesoporous silica supported copper(II) and nickel(II) catalysts for liquid phase oxidation of olefins *Dalton Trans.* **40** 12510
 20. Yadav G D and Lawate Y S 2013 Hydrogenation of Styrene Oxide to 2-Phenyl Ethanol over Polyurea Microencapsulated Mono- and Bimetallic Nanocatalysts: Activity, Selectivity, and Kinetic Modeling *Ind. Eng. Chem. Res.* **52** 4027
 21. Yadav S K and Jeevanandam P 2014 Synthesis of NiO-Al₂O₃ nanocomposites by sol-gel process and their use as catalyst for the oxidation of styrene *J. Alloy. Compd.* **610** 567
 22. Hassan H M A, Saad E M, Soltan M S, Betiha M A, Butler I S and Mostafa S I 2014 A palladium(II) 4-hydroxysalicylidene Schiff-base complex anchored on functionalized MCM-41: An efficient heterogeneous catalyst for the epoxidation of olefins *Appl. Catal. A-Gen.* **488** 148
 23. (a) Vetrivel S, Chen C T and Kao H M 2010 The ultrafast sonochemical synthesis of mesoporous silica MCM-41 *New J. Chem.* **34** 2109; (b) Dehghani S and Haghighi M 2017 Sono-sulfated zirconia nanocatalyst supported on MCM-41 for biodiesel production from sunflower oil: Influence of ultrasound irradiation power on catalytic properties and performance *Ultrason. Sonochem.* **35** 142; (c) Bhunia S, Jana S, Saha D, Dutta B and Koner S 2014 Catalytic olefin epoxidation over cobalt(II)-containing mesoporous silica by molecular oxygen in dimethylformamide medium *Catal. Sci. Technol.* **4** 1820
 24. (a) Shen S, Chen J, Koodali R T, Hu Y, Xiao Q, Zhou J, Wang X and Guo L 2014 Activation of MCM-41 mesoporous silica by transition-metal incorporation for photocatalytic hydrogen production *Appl. Catal. B-Environ.* **150-151** 138; (b) Zhao Q, Zhou X, Ji M, Ding H and Jiang T 2011 Stability and textural properties of cobalt incorporated MCM-48 mesoporous molecular sieve *Appl. Surf. Sci.* **257** 2436
 25. (a) Zhao Q, Zhou X, Ji M, Ding H and Jiang T 2011 Stability and textural properties of cobalt incorporated MCM-48 mesoporous molecular sieve *Appl. Surf. Sci.* **257** 2436; (b) Pradhan A C, Paul A and Rao G R 2017 Sol-gel-cum-hydrothermal synthesis of mesoporous Co-Fe@Al₂O₃-MCM-41 for methylene blue remediation *J. Chem. Sci.* **129** 381
 26. (a) Li B, Zhu Y and Jin X 2015 Synthesis of cobalt-containing mesoporous catalysts using the ultrasonic-assisted "pH-adjusting" method: Importance of cobalt species in styrene oxidation *J. Solid State Chem.* **221** 230; (b) Qi B, Lou L, Wang Y, Yu K, Yang Y and Liu

- S 2014 Comparison of different prepared Mn-MCM-41 catalysts in the catalytic epoxidation of alkenes with 30% H_2O_2 *Micropor. Mesopor. Mat.* **190** 275
27. Zhang Y, Gao F, Wan H, Wu C, Kong Y, Wu X, Zhao B, Dong L and Chen Y 2008 Synthesis, characterization of bimetallic Ce-Fe-SBA-15 and its catalytic performance in the phenol hydroxylation *Micropor. Mesopor. Mat.* **113** 393
 28. (a) Yang F, Zhou S, Gao S, Liu X, Long S and Kong Y 2017 In situ embedding of ultra-fine nickel oxide nanoparticles in HMS with enhanced catalytic activities of styrene epoxidation *Micropor. Mesopor. Mat.* **238** 69; (b) Tong J, Li W, Bo L, Wang H, Hu Y, Zhang Z and Mahboob A 2016 Selective oxidation of styrene catalyzed by cerium-doped cobalt ferrite nanocrystals with greatly enhanced catalytic performance *J. Catal.* **344** 474; (c) Ren S, Yang C, Sun C, Hui Y, Dong Z, Wang J and Su X 2012 Novel NiO nanodisks and hollow nanodisks derived from $Ni(OH)_2$ nanostructures and their catalytic performance in epoxidation of styrene *Mater. Lett.* **80** 23; (d) Kumar P N, Mary J S S, Chandrakala V, Jeyarani W J and Shyla J M, Investigation of superior electro-optical properties of SnO_2/SiO_2 nanocomposite over its individual counterpart SnO_2 nanoparticles *Mater. Chem. Phys.* **193** 234
 29. Ahmed S, Ramli A, Yusup S and Farooq M 2017 Adsorption behavior of tetraethylenepentamine-functionalized Si-MCM-41 for CO_2 adsorption *Chem. Eng. Res. Des.* **122** 33
 30. (a) Wang Y, Liang M, Fang J, Fu J and Chen X 2017 Visible-light photo-Fenton oxidation of phenol with $rGO-\alpha-FeOOH$ supported on Al-doped mesoporous silica (MCM-41) at neutral pH: Performance and optimization of the catalyst *Chemosphere* **182** 468; (b) Cuello N I, Elías V R, Mendieta S N, Longhi M, Crivello M E, Oliva M I and Eimer G A 2017 Drug release profiles of modified MCM-41 with superparamagnetic behavior correlated with the employed synthesis method *Mater. Sci. Eng. C* **78** 674; (c) Ambursa M, Sudarsanam P, Voon L H, Hamid S B A and Bhargava S K 2017 Bimetallic Cu-Ni catalysts supported on MCM-41 and Ti-MCM-41 porous materials for hydrodeoxygenation of lignin model compound into transportation fuels *Fuel Process. Technol.* **162** 87
 31. Guan Y, Wang S, Wang X, Sun C and Huang Y 2017 In situ self-assembled synthesis of Ag-AgBr/Al-MCM-41 with excellent activities of adsorption-photocatalysis *Appl. Catal. B-Environ* **209** 329
 32. (a) Luo S, Fan G, Luo M, Li J and Song G 2016 Synthesis of styrene carbonate from styrene oxide and CO_2 over $ZnBr_2$ supported on MCM-41-Coated magnetic Fe_3O_4 *J. CO₂ Util.* **14** 23; (b) Fan G, Wang Y, Yan J, Song G and Li J 2017 Coupling reaction of carbon dioxide with styrene oxide over $Cu(acac)_2$ and n-Bu₄NBr supported on $Fe_3O_4 @MCM-41$ *J. CO₂ Util.* **18** 370
 33. Fan G Z, Cheng S Q, Zhu M F and Gao X L 2007 Palladium chloride anchored on organic functionalized MCM-41 as a catalyst for the Heck reaction *Appl. Organometal. Chem.* **21** 670
 34. (a) Karthikeyan G and Pandurangan A 2009 Heteropolyacid ($H_3PW_{12}O_{40}$) supported MCM-41: An efficient solid acid catalyst for the green synthesis of xanthenedione derivatives *J. Mol. Catal. A: Chem.* **311** 36; (b) Wang S, Zhang Z, Liu B and Li J 2013 Silica coated magnetic Fe_3O_4 nanoparticles supported phosphotungstic acid: a novel environmentally friendly catalyst for the synthesis of 5-ethoxymethylfurfural from 5-hydroxymethylfurfural and fructose *Catal. Sci. Technol.* **3** 2104
 35. Yang F, Gao S, Xing C, Long S, Li X, Xi T and Kong Y 2015 Direct templating assembly route for the preparation of highly-dispersed vanadia species encapsulated in mesoporous MCM-41 channel *RSC Adv.* **5** 72099
 36. Ma T, Ding J, Shao R, Xu W and Yun Z 2017 Dehydration of glycerol to acrolein over Wells-Dawson and Keggin type phosphotungstic acids supported on MCM-41 catalysts *Chem. Eng. J.* **316** 797
 37. Hussain M M, Rahman M M and Asiri A M 2017 Ultrasensitive and selective 4-aminophenol chemical sensor development based on nickel oxide nanoparticles decorated carbon nanotube nanocomposites for green environment *J. Environ. Sci.* **53** 27
 38. Salavati-Niasari M, Davar F and Fereshteh Z 2010 Synthesis of nickel and nickel oxide nanoparticles via heat-treatment of simple octanoate precursor *J. Alloys Compd.* **494** 410
 39. Hanifehpour Y, Morsali A, Mirtamizdoust B, Joo S W and Soltani B 2017 Thermolysis synthesis of pure phase NiO from novel sonochemical synthesized Ni(II) nano metal-organic supramolecular architecture *Ultrason. Sonochem.* **37** 430
 40. Fang J, Zhang Y, Zhou Y, Zhao S, Zhang C, Huang M and Gao Y 2017 Synthesis of NiO-TiO₂ hybrids/mSiO₂ yolk-shell architectures embedded with ultrasmall gold nanoparticles for enhanced reactivity *Appl. Surf. Sci.* **412** 616
 41. Yang C, Qing Y, An K, Zhang Z, Wang L and Liu C 2017 Facile synthesis of the N-doped graphene/nickel oxide with enhanced electrochemical performance for rechargeable lithium-ion batteries *Mater. Chem. Phys.* **195** 149
 42. (a) Qin J, Li B, Zhang W, Lv W, Han C and Liu J 2015 Synthesis, characterization and catalytic performance of well-ordered mesoporous Ni-MCM-41 with high nickel content *Micropor. Mesopor. Mat.* **208** 181; (b) Wu C, Wang L, Williams P T, Shi J and Huang J 2011 Hydrogen production from biomass gasification with Ni/MCM-41 catalysts: Influence of Ni content *Appl. Catal. B-Environ.* **108-109** 6